Applied Physics Letters

Phase transition of non-Hermitian topological edge states in microwave regime

Cite as: Appl. Phys. Lett. **116**, 211104 (2020); https://doi.org/10.1063/5.0006144
Submitted: 02 March 2020 . Accepted: 05 May 2020 . Published Online: 27 May 2020

Ye Yu, Wange Song, Chen Chen, Tao Chen, Hongmei Ye, Xiaopeng Shen, Qingqing Cheng, and Tao Li

Applied Physics Letters ARTICLE scitation.org/journal/apl

Phase transition of non-Hermitian topological edge states in microwave regime

Cite as: Appl. Phys. Lett. **116**, 211104 (2020); doi: 10.1063/5.0006144
Submitted: 2 March 2020 · Accepted: 5 May 2020 ·
Published Online: 27 May 2020

Ye Yu,[1] Wange Song,[2] Chen Chen,[2] Tao Chen,[1] Hongmei Ye,[3] Xiaopeng Shen,[3] Qingqing Cheng,[1,a)] and Tao Li[2,4,a)]

AFFILIATIONS

[1]School of Optical-Electrical and Computer Engineering, University of Shanghai for Science and Technology, Shanghai 200093, China
[2]National Laboratory of Solid State Microstructures, College of Engineering and Applied Sciences, Nanjing University, Nanjing 210093, China
[3]College of Physical Science and Technology, China University of Mining and Technology, Xuzhou 221116, China
[4]Collaborative Innovation Center of Advanced Microstructures, Nanjing 210093, China

[a)]**Authors to whom correspondence should be addressed:** qqcheng@usst.edu.cn and taoli@nju.edu.cn

ABSTRACT

Recent advances in non-Hermitian topological phases have exploited the unusual features in photonics systems. In particular, the coupling effect and parity–time (PT) symmetry have been found to jointly determine the transition of topological edge states, which have yet to be detected directly in coupled PT-symmetric waveguides. In this work, we use a finite waveguide array described by the Su–Schrieffer–Heeger model to explicitly reveal the relation between the topological states and PT symmetry and unveil the condition for the coexistence of topological edge states and PT phases. Microwave-near-field experiments have revealed non-trivial edge states in both exact- and broken-PT phases in ultrathin corrugated metallic coupled waveguide arrays. This work thus establishes an integrated microwave waveguide platform based on which more interesting physics and functional devices related to topological photonics and PT symmetry may be developed.

In photonics, topological insulators have attracted significant interest since a series of topological phenomena in non-electronic systems were proposed and demonstrated a few years ago in periodic time-reversal-breaking magneto-optical devices.[1–4] Subsequently, intense theoretical and experimental works have been devoted to realizing topological edge states (TESs) in a variety of photonic systems, such as photonic crystals,[3,4] semiconductor quantum wells,[5] arrays of coupled resonators,[6–10] metamaterials,[11] and polaritons in microcavities.[12–14] Also note that waveguide array[7,15–20] is increasingly becoming an important platform for research into TESs. Various photonic waveguides already play important technological roles, such as the spoof surface plasmon polariton (SSPP) waveguides, which are widely used in broadband and high-efficiency converters,[21–23] frequency splitters,[24,25] and wavelength demultiplexers.[26,27] To further extend the research on SSPPs into topological photonics, a microwave photonics system consisting of ultrathin corrugated metallic coupled waveguides was used to imitate the Su–Schrieffer–Heeger (SSH) model. This work immediately generated a remarkable interest in various phenomena, such as generally localized modes in the modified SSH model[28,29] and Floquet π modes in the dynamic SSH model.[30]

Although the ideas of topology have found tremendous success in closed physical systems, an even richer set of properties exist in the more general open or non-Hermitian framework.[31–33] Non-hermiticity and parity–time (PT) symmetry have triggered tremendous research interest over the past decades.[31–36] The eigenvalues of a PT-symmetric Hamiltonian can be purely real within an exact-PT phase and transform to complex values upon crossing a degeneracy (i.e., an exceptional point where the eigenvectors and not just eigenvalues are degenerate).[31,37–39] Of the various PT-symmetric systems,[34,35,40–43] PT photonics has become attractive because it is conveniently achievable to design potential-PT-symmetric systems with intentionally modulated gain and loss.[44] Such systems allow fundamental notions linked with non-Hermiticity to be explored based on a photonics platform.[32,36] In addition, a series of interesting optical phenomena and devices, such as unidirectional light reflection,[45] PT-symmetry-breaking lasers,[6,46] and sensitivity enhanced by exceptional points,[47–49] have been realized by exploiting PT symmetry. Inspired by these interesting effects, numerous research efforts have attempted to widen the scope of non-Hermitian optics by incorporating non-Hermitian features into topological systems.[6–9,32,50,51] For example,

non-Hermitian SSH photonic lattices have been developed and their effects were experimentally confirmed, such as non-Hermitian-enhanced or -induced topological states,[51,52] one-dimensional topological lasers,[6,7] topological transitions,[16,53] and the recovery of exact-zero modes.[54] However, because loss modulation is difficult in SSPP waveguides, few studies have investigated topological photonics with PT symmetry in microwave plasmonic waveguide arrays.

By using a cladding film with contrast loss, this work experimentally demonstrates the passive PT-symmetric dissipation of SSPPs in an ultrathin corrugated metallic array of coupled microwave waveguides. By varying the gain–loss profile and coupling coefficient, we construct a topological–PT phase diagram to illustrate transitions both from exact- to broken-PT phases and from trivial to non-trivial topological states. Our theoretical results are verified by the results of microwave-near-field experiments using coupled metal-clad waveguides in which the microwave waveguides are designed to mimic the SSH model with passive PT-symmetric dissipation. This coupled microwave waveguide array provides a versatile platform for investigating various phenomena related to PT symmetry, such as non-Hermitian skin effects,[55–57] non-Hermitian chiral damping,[56,58] and PT-symmetric flat bands.[4,59]

The SSH model describes a one-dimensional (1D) topological structure with intra- and intercell hopping of variable strength. Figure 1(a) shows a schematic diagram of a 1D SSH modeled photonics lattice with N coupled gain–loss waveguides consisting of an array of ultrathin corrugated metallic coupled waveguides. The corrugated metallic waveguide supports SSPPs from the microwave to the infrared range. Following coupled-mode theory in the tight-binding approximation, the propagation of electromagnetic fields within the waveguide array is described as

$$\begin{aligned} -i\frac{\partial}{\partial x}\varphi_n &= \beta_L\varphi_n + c_1\varphi_{n-1} + c_2\varphi_{n+1}, \quad n = 1, 3, \ldots, \\ -i\frac{\partial}{\partial x}\varphi_n &= \beta_G\varphi_n + c_2\varphi_{n-1} + c_1\varphi_{n+1}, \quad n = 2, 4, \ldots, \end{aligned} \tag{1}$$

where the parameters c_1 and c_2 are the intra- and intercell coupling coefficients, β_L and β_G (with $\beta_L = \beta + i\gamma$, $\beta_G = \beta - i\gamma$, where γ is the gain or loss strength) are the on-site propagation constants in the lossy and gain waveguides, respectively, $n = 1, 2, 3, \ldots, N$ enumerates the waveguides, and φ_n is the mode field in waveguide n. For simplicity, we first consider $c_1 = c_2 \equiv c$, which is the coupling between straight, uniform waveguides. In this case, the system supports either exact- or broken-PT phases, depending on the magnitude of the coupling coefficient c compared with the gain–loss strength γ. If c increases with γ fixed, the system undergoes a phase transition from the broken- to exact-PT phase at the threshold coupling strength c_{PT}.[33] Figure 1(b) shows that the ratio c_{PT}/γ is linear in N.

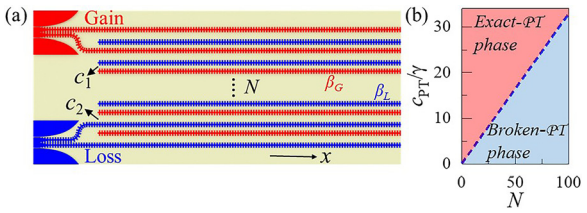

FIG. 1. Model of the 1D finite non-Hermitian waveguide array and topological–PT phase diagram. (a) Schematic diagram of the 1D finite non-Hermitian SSH model with N lattices, where red and blue indicate gain and loss, respectively, β_G and β_L are the on-site propagation constants (where $\beta_L = \beta + i\gamma$, $\beta_G = \beta - i\gamma$, where γ is the gain or loss strength), and c_1 and c_2 are the coupling coefficients of the dimerized chain. (b) The ratio c_{PT}/γ as a function of N with $c_1 = c_2 \equiv c$.

We now consider the SSH model ($c_1 \neq c_2$). For the Hermitian case ($\gamma = 0$), the ratio c_1/c_2 determines the topological phases: $c_1/c_2 < 1$ corresponds to the topologically trivial phase, whereas $c_1/c_2 > 1$ corresponds to the non-trivial phase that supports TESs. For the non-Hermitian case, the global Berry phase (Φ_{GB}) is used to probe the topological nature,[60,61] corresponding in our case to the summation of the Berry phase of both the lower and upper bands (i.e., $\Phi_{GB} = \Phi_B^1 + \Phi_B^2$). The Berry phase in each band is $\Phi_B^m = \oint_k idk\langle\psi_m(k)|\frac{\partial}{\partial k}|\psi_m(k)\rangle$, where $m = 1, 2$ is the band number, ψ_m is the eigenstate, and k is the Bloch wavenumber in the first Brillouin zone. This expression can be simplified in our system to $\Phi_B^m = \Phi_0/2 \pm \frac{1}{2}\oint_{\phi_k} \cos\gamma_k d\phi_k$, where $\gamma_k = \arctan[|c_1 + c_2\exp(-iak)|/i\gamma]$, $\arg[c_1 + c_2\exp(-iak)] = \phi_k$, and a is the lattice constant.[51] This equation clearly expresses the intrinsic Berry phase in the Hermitian case (i.e., $\Phi_0/2$) and the non-Hermitian-induced geometric phase. Note that the global Berry phase remains quantized regardless of the on-site non-Hermitian modulation in our system (i.e., $\Phi_{GB} = \Phi_B^1 + \Phi_B^2 = \Phi_0$), revealing the same topological nature as Hermitian systems. Although the topological phase does not change, the quantum phase can be dramatically modified by the non-Hermitian parameters, which can also give rise to intriguing topological characteristics, for example, the topologically protected zero-energy modes.[51,52] Combining the TES with non-Hermiticity produces two types of edge states: one type in the exact-PT phase and the other type in the broken-PT phase.[51,54] The transition between these two edge states has been demonstrated by non-Hermitian[60] modulation (i.e., gain and loss) and by tuning the system size.[54]

To more clearly and elaborately reveal the relation between PT phases and topological phases, we show in Fig. 2(a) a topological–PT phase diagram in the parametric space of c_1/c_2, c_2/c_{PT}, and N. The blue plane is defined by $c_1/c_2 = 1$ and separates the TES phases into topologically trivial and non-trivial, and the red surface separates the PT phases. These two surfaces intersect at the dashed line $c_1/c_2 = 1$, $c_2/c_{PT} = 1$ and give rise to four different phase regions in the diagram: **I**, exact-PT and topologically non-trivial phases; **II**, broken-PT and topologically non-trivial phases; **III**, broken-PT and topologically trivial phases; and **IV**, exact-PT and topologically trivial phases. Figure 2(b) shows the section of the phase diagram at $N = 12$, which reveals four phase regions. The non-trivial phase ($c_1/c_2 > 1$) is distinguished by two regions, one with the exact-PT phase **I** and the other with the broken-PT phase **II**. The edge states in the non-trivial phase are correspondingly divided into two categories: those in the exact-PT phase **I** and those in the broken-PT phase **II**. The two edge states in the exact-PT phase have split near-zero mode constants. The field intensity profiles are identical, although they have different real and imaginary components (see Sec. A of the supplementary material). Thus, the electric fields of these states evolve in the same way in the waveguides, with the field localized at both boundaries, as shown in Fig. 2(c) for the parameters $c_1/c_2 = 2$, $c_2/c_{PT} = 20$. However, the two non-trivial edge states in the broken-PT phase in region **II** have zero mode constants with the field localized at only one boundary, depending on the loss or gain, because of the broken-PT symmetry, as shown in

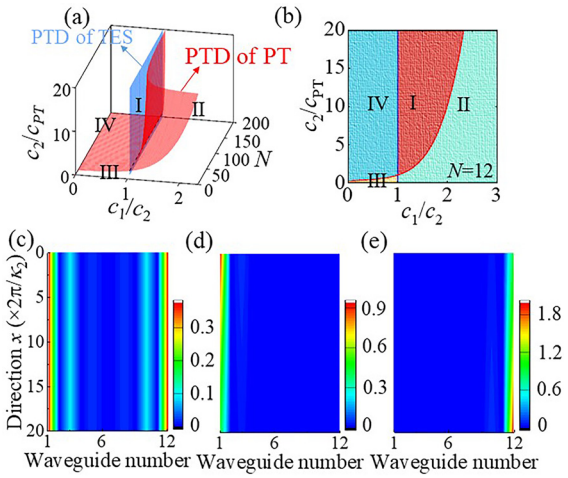

FIG. 2. Topological–PT phase diagram. (a) Phase diagram in the parameter space of (c_1/c_2, c_2/c_{PT}, N) revealing PT and topological properties: **I**, exact-PT and topologically non-trivial phases; **II**, broken-PT and topologically non-trivial phases; **III**, broken-PT and topologically trivial phases; and **IV**, exact-PT and topologically trivial phases. The dashed line indicates the intersection of the blue and red surfaces. (b) Phase diagram in the parameter plane of (c_1/c_2, c_2/c_{PT}) with $N = 12$. Field evolutions of the topological edge states with (c) the exact-PT phase with the parameters of $c_1/c_2 = 2$ and $c_2/c_{PT} = 20$ and (d) and (e) the broken-PT phase with the parameters of $c_1/c_2 = 4$, $c_2/c_{PT} = 20$ as they propagate in the x direction.

Figs. 2(d) and 2(e) for the parameters $c_1/c_2 = 4$, $c_2/c_{PT} = 20$. Compared with the edge states in the exact-PT phase, the edge states in the broken-PT phase are more robust because of the exact-zero mode constants.[54] Further details of the edge states in different PT phases are provided in Sec. B of the supplementary material.

To confirm these theoretical results, we experimented with the transmitting microwaves through spoof plasmonic waveguide arrays, which constitute passive PT-symmetric microwave systems. To realize a microwave plasmonic system, the key parameter in our experiments was the processing contrast loss of the metallic microwave waveguides. However, in the microwave-frequency range, almost all metals are good conductors. Fortunately, the conductive properties of tin and copper are very different, which means that the losses between these two metals differ significantly. We first measured the attenuation coefficient for SSPP propagation through a waveguide clad in tin or copper. Two single "H-shaped" metallic waveguides with tin-coated copper and pure copper layers (thickness is 0.018 mm) were fabricated on a printed circuit board (F4BK), with a dielectric constant of 2.65, a loss tangent of 0.001, and a thickness of 0.2 mm [see Fig. 3(a)]. The distribution of the electric-field amplitude was obtained by using a near-field test platform [see the supplementary material Fig. S3(a)], which is composed of a Vector Network Analyzer (VNA, model E5063A), a monopole antenna as the detector, and automated translation stages controlled by a stepper motor to translate in the x and y directions. The input of the waveguide is connected to port 1 of the VNA through a Subminiature version A (SMA) cable to input energy, and the waveguide output is adhered to an absorber to eliminate reflections. In addition, the antenna detector connected to port 2 of the VNA is positioned 1.4 mm from the metallic waveguide to probe the amplitude distribution of the vertical electric-field component E_z.

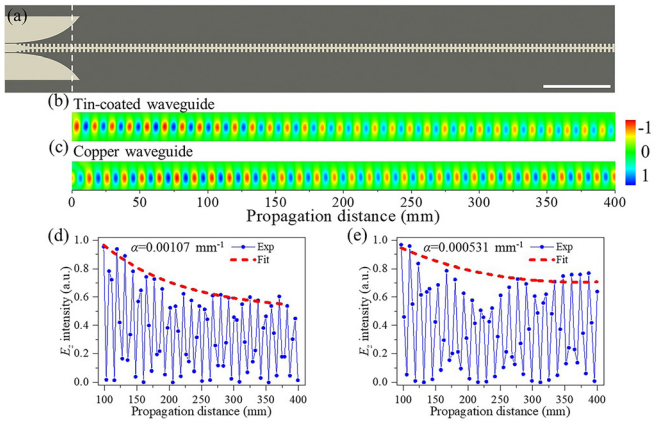

FIG. 3. Experimental measurements of amplitude attenuation coefficients. (a) Schematic illustration of the H-shaped metallic waveguide with the white scale bar of 50 mm. Experimentally mapped near-field E_z distributions through a single copper waveguide (b) with and (c) without the tin-coated film. The amplitude of E_z as a function of propagation distance through a single copper waveguide (d) with and (e) without the tin-coated film.

Figure 3(a) shows the near-field distribution of E_z at the microwave frequency of 17 GHz through a single H-shaped metallic waveguide, and Figs. 3(b) and 3(c) show the same for tin-coated copper and pure copper waveguides, respectively, as recorded by our near-field platform. The SSPP amplitudes clearly experience different losses along the 400-mm-long waveguides, as shown in Figs. 3(d) and 3(e). From these results, we derive the amplitude-attenuation coefficients α, which are 0.00 107 mm^{-1} for the tin-coated copper waveguide [Fig. 3(d)] and 0.00 0531 mm^{-1} for the copper waveguide [Fig. 3(e)].

Another key parameter is the coupling strength, which corresponds to the hopping term in the SSH model. According to the weak-guidance approximation, the nearest-neighbor coupling strength c depends primarily on the nearest-neighbor separation d. The results show that the coupling strengths vary from 0.0984 to 0.0224 mm^{-1} as a function of the spacing between adjacent waveguides (from 1 to 4.2 mm; see the supplementary material Fig. S4). We next fabricated arrays of six straight waveguides made of (i) copper coated with tin and (ii) pure copper. These waveguide arrays were fabricated on a flexible circuit board (F4BK) with a dielectric constant of 2.65, and both waveguides had spacings of $d_1 + d_2$ [these parameters are shown in Fig. 4(b); see also Fig. S3(b) of the supplementary material for a photograph of the samples]. We then combined these waveguide arrays upside down to form an F4BK-metallic waveguide–F4BK sandwich structure. The nearest-neighbor tin-coated copper (pure copper) waveguides introduce periodic loss modulation with a field attenuation coefficient of $\alpha = 0.00\,107$ mm^{-1} ($\alpha = 0.000\,531$ mm^{-1}) at 17 GHz. Therefore, the pure copper waveguides (i.e., with no tin coating) provide "gain" leading to a relative loss offset of $2\gamma = 0.000\,539$ mm^{-1}.

Furthermore, to produce a TES eigenmode, both the intensity and phase of the initial state should be carefully prepared. In fact, the TES consists of a complex distribution in intensity and phase (see the supplementary material Fig. S1), which are difficult to prepare with precision in experiments. Here, we approximately produce the TES eigenmode by engineering the intensity and phase of four waveguides, which was done by designing two branch waveguides [see Fig. 4(a);

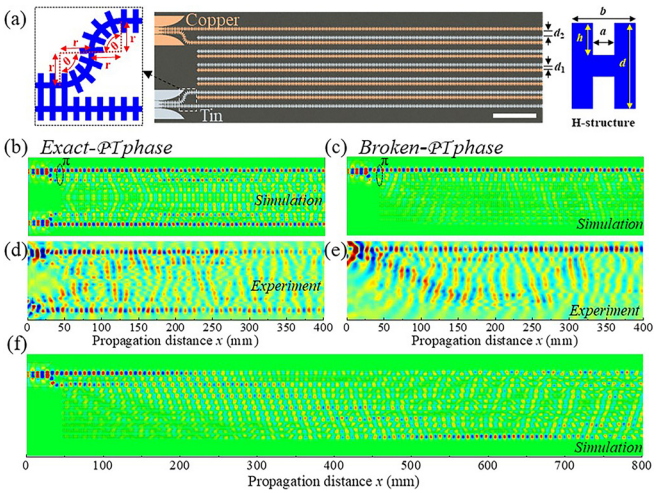

FIG. 4. Experimental demonstration of the TES and PT phase transition. (a) Schematic diagram of straight plasmonic waveguide arrays with the H-shaped structure with initial state control. The expanded view at right shows details of the structure and of the input ports. The white scale bar is 50 mm. (b) and (c) Numerical results of full-wave simulations. (b) Exact-PT phase with boundary excitation. (c) Broken-PT phase with boundary excitation. (d) and (e) Corresponding experimentally mapped electric-near-field distribution within the SSPP waveguide array. (f) Comparison of the exact-PT phase with excitation in the branching waveguides. The elliptical circles in panels (b) and (d) show the π phase difference.

one waveguide is straight and the other contains two 4.67-mm-radius arcs with $\theta = 1.68$ rad for the exact-PT phase]. A π phase difference between the two branches can be obtained as required by the edge-mode field distribution (see Sec. C of the supplementary material). Figure 4(a) shows the 12 waveguides and the structural parameters d, a, h, and b of the H-shape and of the gaps (d_1 and d_2). The parameters were optimized at $d = 4$ mm, $a = 1$ mm, $h = 1.5$ mm, $b = 3$ mm, $d_1 = 2.2$ mm, and $d_2 = 4.2$ mm. Based on this design, the waveguide array has two coupling coefficients, $c_1 = 0.0520\,\mathrm{mm}^{-1}$ and $c_2 = 0.0224\,\mathrm{mm}^{-1}$, which give $c_1/c_2 = 2.32$ and $c_2/c_{\mathrm{PT}} = 20.0$ and place this device in region **I** [here, $c_{\mathrm{PT}} = 0.00112\,\mathrm{mm}^{-1}$ according to Fig. 1(b)]. The experimental amplitude mapping indicates a good boundary mode with the exact-PT symmetry [Fig. 4(d)]. For comparison, a controlled excitation in the branching waveguides exhibits scattering into the bulk waveguides and tends to couple to another boundary mode rather than being localized at the original boundary waveguides for the exact-PT phase [see Fig. 4(f)], which is quite different from the localized boundary mode shown in Figs. 4(b) and 4(d).

The TES in the broken-PT phase is also verified with the parameters $c_1/c_2 = 3.49$ and $c_2/c_{\mathrm{PT}} = 20.0$. Here, we maintain $2\gamma = 0.000\,539\,\mathrm{mm}^{-1}$ (so $c_{\mathrm{PT}} = 0.00\,112\,\mathrm{mm}^{-1}$ remains unchanged) and $c_2 = 0.0224\,\mathrm{mm}^{-1}$ and change c_1 to $0.0781\,\mathrm{mm}^{-1}$ (corresponding to $d_1 = 1.4$ mm). Figure 4(e) shows the distribution E_z of the electric-field amplitude for the initial TES eigenmode control ($r = 3.92$ mm and $\theta = 1.80$ rad; see the supplementary material Table S1). The controlled excitation produces relatively good single-boundary confinement for the broken-PT phase, indicating a good TES in spite of the slight noise inside the whole lattice. Note that the scattered fields in Fig. 4(e) may be attributed to the scattering from the arcs of the input structures but not to the intrinsic imperfections inside the waveguides. Nevertheless, these experimental results on the exact-PT and broken-PT phases are entirely consistent with the numerical simulations done using the commercial full-wave solver Computer Simulation Technology (CST) Microwave Studio, with all parameters used in the simulations derived from the experimental data. As expected, the simulation results are consistent with the experimental results [see Figs. 4(b) and 4(c)].

In conclusion, this work experimentally demonstrates that topological non-trivial exact- and broken-PT phases are supported in a finite non-Hermitian system. Two types of edge states that exist in different PT phases are explicitly visualized by microwave-near-field characterization and CST full-wave simulations in a finite SSH-type PT-symmetric SSPP waveguide array. The experimental results directly reveal the different eigenmodes and evolution of the TESs in the different PT phases. This demonstration enriches the research scope of the PT symmetry and establishes a platform for microwave waveguide arrays with passive PT-symmetric dissipation that may significantly impact research into interesting effects and functionalities related to topological and PT photonics.

AUTHORS' CONTRIBUTIONS

Y.Y. and W.S. contributed equally to this work.

See the supplementary material for the studied topological edge states.

This work was supported by the National Key R&D Program of China (Grant Nos. 2017YFA0303701 and 2016YFA0202103), the National Natural Science Foundation of China (Grant Nos. 11874266, 11604208, 11674167, 11621091, 91850204, and 61372048), the Dengfeng Project B of Nanjing University, and the Shanghai Science and Technology Committee (Grant Nos. 16ZR1445600 and 17CG49).

DATA AVAILABILITY

The data that support the findings of this study are available from the corresponding authors upon reasonable request.

REFERENCES

[1]T. Ozawa, H. M. Price, A. Amo, N. Goldman, M. Hafezi, L. Lu, M. C. Rechtsman, D. Schuster, J. Simon, and O. Zilberberg, Rev. Mod. Phys. **91**, 015006 (2019).
[2]I. L. Garanovich, S. Longhi, A. A. Sukhorukov, and Y. S. Kivshar, Phys. Rep. **518**, 1 (2012).
[3]Z. Wang, Y. Chong, J. D. Joannopoulos, and M. Soljačić, Nature **461**, 772 (2009).
[4]F. Haldane and S. Raghu, Phys. Rev. Lett. **100**, 013904 (2008).
[5]N. H. Lindner, G. Refael, and V. Galitski, Nat. Phys. **7**, 490 (2011).
[6]H. Zhao, P. Miao, M. H. Teimourpour, S. Malzard, R. El-Ganainy, H. Schomerus, and L. Feng, Nat. Commun. **9**, 981 (2018).
[7]M. Parto, S. Wittek, H. Hodaei, G. Harari, M. A. Bandres, J. Ren, M. C. Rechtsman, M. Segev, D. N. Christodoulides, and M. Khajavikhan, Phys. Rev. Lett. **120**, 113901 (2018).
[8]G. Harari, M. A. Bandres, Y. Lumer, M. C. Rechtsman, Y. D. Chong, M. Khajavikhan, D. N. Christodoulides, and M. Segev, Science **359**, eaar4003 (2018).
[9]M. A. Bandres, S. Wittek, G. Harari, M. Parto, J. Ren, M. Segev, D. N. Christodoulides, and M. Khajavikhan, Science **359**, eaar4005 (2018).
[10]F. Gao, Z. Gao, X. Shi, Z. Yang, X. Lin, H. Xu, J. D. Joannopoulos, M. Soljačić, H. Chen, and L. Lu, Nat. Commun. **7**, 11619 (2016).

[11]H. Jia, R. Zhang, W. Gao, Q. Guo, B. Yang, J. Hu, Y. Bi, Y. Xiang, C. Liu, and S. Zhang, Science **363**, 148 (2019).
[12]D. Smirnova, S. Kruk, D. Leykam, E. Melik-Gaykazyan, D.-Y. Choi, and Y. Kivshar, Phys. Rev. Lett. **123**, 103901 (2019).
[13]S. Kruk, A. Poddubny, D. Smirnova, L. Wang, A. Slobozhanyuk, A. Shorokhov, I. Kravchenko, B. Luther-Davies, and Y. Kivshar, Nat. Nanotechnol. **14**, 126 (2019).
[14]A. Slobozhanyuk, S. H. Mousavi, X. Ni, D. Smirnova, Y. S. Kivshar, and A. B. Khanikaev, Nat. Photonics **11**, 130 (2017).
[15]M. C. Rechtsman, J. M. Zeuner, Y. Plotnik, Y. Lumer, D. Podolsky, F. Dreisow, S. Nolte, M. Segev, and A. Szameit, Nature **496**, 196 (2013).
[16]J. M. Zeuner, M. C. Rechtsman, Y. Plotnik, Y. Lumer, S. Nolte, M. S. Rudner, M. Segev, and A. Szameit, Phys. Rev. Lett. **115**, 040402 (2015).
[17]S. Weimann, M. Kremer, Y. Plotnik, Y. Lumer, S. Nolte, K. G. Makris, M. Segev, M. C. Rechtsman, and A. Szameit, Nat. Mater. **16**, 433 (2017).
[18]Y. Ke, X. Qin, F. Mei, H. Zhong, Y. S. Kivshar, C. J. L. Lee, and P. Reviews, Laser Photonics Rev. **10**, 995 (2016).
[19]C. Han, M. Lee, S. Callard, C. Seassal, and H. Jeon, Light: Sci. Appl. **8**, 40 (2019).
[20]Q. Cheng, Y. Pan, Q. Wang, T. Li, and S. Zhu, Laser Photonics Rev. **9**, 392 (2015).
[21]W. Sun, Q. He, S. Sun, and L. Zhou, Light: Sci. Appl. **5**, e16003 (2016).
[22]X. Shen and T. J. Cui, Laser Photonics Rev. **8**, 137 (2014).
[23]H. F. Ma, X. Shen, Q. Cheng, W. X. Jiang, and T. J. Cui, Laser Photonics Rev. **8**, 146 (2014).
[24]X. Gao, L. Zhou, Z. Liao, H. F. Ma, and T. J. Cui, Appl. Phys. Lett. **104**, 191603 (2014).
[25]X. Gao, J. H. Shi, X. Shen, H. F. Ma, W. X. Jiang, L. Li, and T. J. Cui, Appl. Phys. Lett. **102**, 151912 (2013).
[26]X. Gao, W. Che, and W. Feng, Sci. Rep. **8**, 2456 (2018).
[27]Y. J. Zhou and B. J. Yang, Opt. Express **22**, 21589 (2014).
[28]Q. Cheng, T. Chen, D. Yu, Y. Liao, J. Xie, X. Zang, X. Shen, and Y. Pan, Opt. Express **26**, 31636 (2018).
[29]T. Chen, Y. Yu, Y. Song, D. Yu, H. Ye, J. Xie, X. Shen, Y. Pan, and Q. Cheng, Ann. Phys. **531**, 1900347 (2019).
[30]Q. Cheng, Y. Pan, H. Wang, C. Zhang, D. Yu, A. Gover, H. Zhang, T. Li, L. Zhou, and S. Zhu, Phys. Rev. Lett. **122**, 173901 (2019).
[31]C. M. Bender and S. Boettcher, Phys. Rev. Lett. **80**, 5243 (1998).
[32]C. E. Rüter, K. G. Makris, R. El-Ganainy, D. N. Christodoulides, M. Segev, and D. Kip, Nat. Phys. **6**, 192 (2010).
[33]Ş. Özdemir, S. Rotter, F. Nori, and L. Yang, Nat. Mater. **18**, 783 (2019).
[34]M. Kalasad, M. Rabinal, and B. Mulimani, J. Phys. D **43**, 305301 (2010).
[35]Y. N. Joglekar and B. Bagchi, J. Phys. A **45**, 402001 (2012).
[36]Y. N. Joglekar and A. K. Harter, Photonics Res. **6**, A51 (2018).
[37]C. M. Bender, Rep. Prog. Phys. **70**, 947 (2007).
[38]S. Klaiman, U. Günther, and N. Moiseyev, Phys. Rev. Lett. **101**, 080402 (2008).
[39]A. Guo, G. Salamo, D. Duchesne, R. Morandotti, M. Volatier-Ravat, V. Aimez, G. Siviloglou, and D. Christodoulides, Phys. Rev. Lett. **103**, 093902 (2009).
[40]C. M. Bender, D. C. Brody, and H. F. Jones, Phys. Rev. D **70**, 025001 (2004).
[41]I. Rotter, J. Phys. A **42**, 153001 (2009).
[42]N. Chtchelkatchev, A. Golubov, T. Baturina, and V. Vinokur, Phys. Rev. Lett. **109**, 150405 (2012).
[43]C. Hang, G. Huang, and V. V. Konotop, Phys. Rev. Lett. **110**, 083604 (2013).
[44]R. El-Ganainy, K. Makris, D. Christodoulides, and Z. H. Musslimani, Opt. Lett. **32**, 2632 (2007).
[45]L. Feng, Y.-L. Xu, W. S. Fegadolli, M.-H. Lu, J. E. Oliveira, V. R. Almeida, Y.-F. Chen, and A. Scherer, Nat. Mater. **12**, 108 (2013).
[46]L. Feng, Z. J. Wong, R.-M. Ma, Y. Wang, and X. Zhang, Science **346**, 972 (2014).
[47]W. Chen, Ş. K. Özdemir, G. Zhao, J. Wiersig, and L. Yang, Nature **548**, 192 (2017).
[48]Y.-H. Lai, Y.-K. Lu, M.-G. Suh, Z. Yuan, and K. Vahala, Nature **576**, 65 (2019).
[49]M. P. Hokmabadi, A. Schumer, D. N. Christodoulides, and M. Khajavikhan, Nature **576**, 70 (2019).
[50]B. Midya, H. Zhao, and L. Feng, Nat. Commun. **9**, 2674 (2018).
[51]M. Pan, H. Zhao, P. Miao, S. Longhi, and L. Feng, Nat. Commun. **9**, 1308 (2018).
[52]K. Takata and M. Notomi, Phys. Rev. Lett. **121**, 213902 (2018).
[53]M. Bellec, U. Kuhl, G. Montambaux, and F. Mortessagne, Phys. Rev. Lett. **110**, 033902 (2013).
[54]W. Song, W. Sun, C. Chen, Q. Song, S. Xiao, S. Zhu, and T. Li, Phys. Rev. Lett. **123**, 165701 (2019).
[55]C. H. Lee and R. Thomale, Phys. Rev. B **99**, 201103 (2019).
[56]S. Longhi, Phys. Rev. Res. **1**, 023013 (2019).
[57]H. Wang, J. Ruan, and H. Zhang, Phys. Rev. B **99**, 075130 (2019).
[58]Z. Gong, Y. Ashida, K. Kawabata, K. Takasan, S. Higashikawa, and M. Ueda, Phys. Rev. X **8**, 031079 (2018).
[59]H. Zhou, J. Y. Lee, S. Liu, and B. Zhen, Optica **6**, 190 (2019).
[60]S.-D. Liang and G.-Y. Huang, Phys. Rev. A **87**, 012118 (2013).
[61]S. Lieu, Phys. Rev. B **97**, 045106 (2018).